High-Resolution 160-GHz Imaging MIMO Radar Using MMICs With On-Chip Frequency Synthesizers

André Dürr, *Student Member, IEEE*, Dominik Schwarz, Stephan Häfner, Martin Geiger, *Graduate Student Member, IEEE*, Fabian Roos, *Student Member, IEEE*, Martin Hitzler, *Member, IEEE*, Philipp Hügler, *Student Member, IEEE*, Reiner Thomä, *Fellow, IEEE*, and Christian Waldschmidt, *Senior Member, IEEE*

***Abstract*— A high-resolution frequency-modulated continuous wave imaging radar for short-range applications is presented. A range resolution of about 1 cm is achieved with a bandwidth of up to 16 GHz around 160 GHz. In order to overcome losses and large tolerances on a printed circuit board (PCB), eight coherently coupled monolithic microwave integrated circuits (MMICs) are used, each with one transmit and receive antenna on-chip and each representing a single-channel radar system. The signals on the PCB are below 12 GHz, which facilitates fabrication and enables a design with low-cost substrates. The MMIC comprises a phase noise (PN)-optimized architecture with a fully integrated on-chip frequency synthesizer. Due to partly uncorrelated PN between the frequency synthesizer components, the noise level is increased in bistatic radar measurements between two different MMICs, which is explained by a thorough PN analysis. Time-division multiplexing is used to realize a multiple-input multiple-output system with a virtual array of 64 elements and an angular resolution better than 1.5° for the designed array. The positioning tolerances of the MMICs are included into the design resulting in a robust array design. The high-resolution radar performance is proven by imaging radar measurements of two exemplary scenarios.**

***Index Terms*— Frequency-modulated continuous wave (FMCW) radar, imaging radar, mm-wave radar, multiple-input multiple-output (MIMO) radar, phase noise (PN), sparse antenna arrays.**

I. Introduction

RADAR sensors are widely used for industrial, medical, security, and automotive applications [1]. There is a growing demand for high-resolution short-range imaging radar sensors measuring range, velocity, and angle in harsh environments. This leads to more information about the scene under investigation, but requires a high absolute bandwidth and, therefore, pushes frequencies above 100 GHz.

TABLE I
Overview of mm-Wave Imaging Radar Systems

Source	f_{max}	AoC	# Virt. ch.	BW	$\Delta\varphi/\Delta\theta$
[11]	77 GHz	no	16	2 GHz	12°/–
[12]	77 GHz	no	256	2 GHz	6°/6°
[13]	79 GHz	no	16	7 GHz	2°/2°
[14]	100 GHz	no	484	10 GHz	0.3°/0.3°
[15]	120 GHz	no	16	5 GHz	3°/21°
[16]	140 GHz	yes	12	20 GHz	5°/–
This work	160 GHz	yes	64	16 GHz	1°/–

The progress in the low-cost silicon–germanium (SiGe) technology provoked the development of radar monolithic microwave integrated circuits (MMICs) based on the frequency-modulated continuous wave (FMCW) principle. Above 100 GHz, it is desirable to integrate voltage-controlled oscillators (VCOs), amplifiers, mixers, and couplers on the MMIC. By additionally integrating antennas on-chip (AoCs), lossy and complicated high-frequency transitions to printed circuit board (PCB) antennas are avoided. In the past years, several single-channel radar systems fully integrated on an MMIC with AoCs were presented [2]–[7].

Imaging radars are well-known and numerous ones have been introduced [8]–[13]. Table I is ordered by the maximum operating frequency f_{max} and gives an overview of already presented mm-wave FMCW imaging radar systems and their theoretical angular resolution above 77 GHz. In [14]–[16], radar systems at 100 GHz or above are presented.

In [14] and [15], imaging radar systems are realized using an optimized 2-D sparse array. The system concept is based on separate transmit (TX) and receive (RX) modules with a frequency multiplier approach. The local oscillator (LO) is derived from a single phase-locked loop (PLL). The antennas are realized on a PCB due to the considerably lower frequency range at approximately 100 and 120 GHz in comparison with the 160 GHz in this paper.

In addition, Table I shows that only [15] and [16] are realized distinctly above 100 GHz. The system architecture

Manuscript received December 19, 2018; revised February 4, 2019 and February 18, 2019; accepted February 24, 2019. Date of publication April 9, 2019; date of current version September 4, 2019. This work was supported by the Deutsche Forschungsgemeinschaft (DFG, Germany Research Foundation) under Project 317632307. *(Corresponding author: André Dürr.)*

The authors are with the Institute of Microwave Engineering, Ulm University, 89081 Ulm, Germany, and also with the Electronic Measurements and Signal Processing Group, Technische Universität Ilmenau, 98693 Ilmenau, Germany (e-mail: andre.duerr@uni-ulm.de).

Color versions of one or more of the figures in this article are available online at http://ieeexplore.ieee.org.

Digital Object Identifier 10.1109/TMTT.2019.2906176

0018-9480 © 2019 IEEE. Translations and content mining are permitted for academic research only. Personal use is also permitted, but republication/redistribution requires IEEE permission. See http://www.ieee.org/publications_standards/publications/rights/index.html for more information.

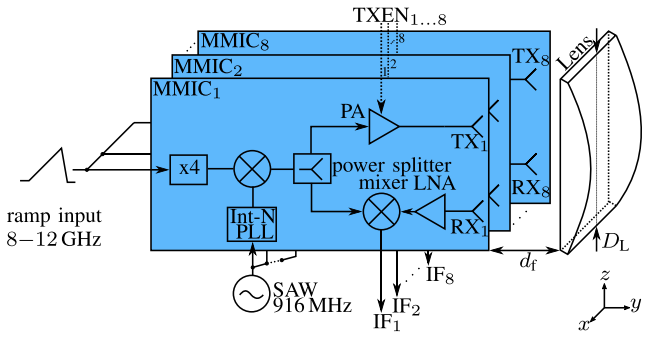

Fig. 1. Block chart of the realized RF front end with the functional principle of a single-channel radar MMIC. Each MMIC is switched ON with a TXEN.

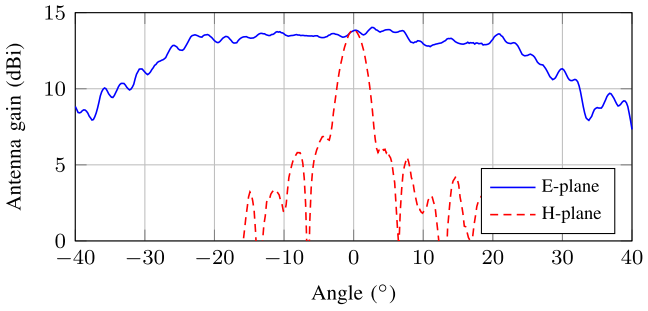

Fig. 2. Measured radiation pattern for the realized spherical-convex lens antenna at 154 GHz.

in [16] is based on a frequency multiplier with factor 8 and is comparable to [14] and [15], but it uses AoCs.

By combining several single-channel MMICs to one system, a 160-GHz imaging radar can be realized. The full integration of the whole radar system on the MMIC including the antennas results in antenna spacings of several wavelengths. In addition, the antenna array at frequencies above 100 GHz is sensitive to positioning tolerances, which demands to include them into the array design process. In comparison with previous systems, this paper contains two new key aspects.

First, the MMIC comprises a radar system with a phase noise (PN) optimized system architecture for single-channel applications. This paper discusses whether this architecture is also advantageous for multichannel applications. The investigation is based on a thorough PN analysis. Second, this paper presents an optimization approach allowing to integrate manufacturing tolerances into the array design.

This paper is organized as follows. After describing the system setup, a thorough PN analysis of the radar system is presented and proven by measurements in Section II. An adapted array design process including manufacturing tolerances is discussed in Section III. The limits concerning the angular performance of the realized radar system are studied in Section IV. Finally, the imaging capabilities of the developed radar are demonstrated in Section V in two typical nonstationary scenarios.

II. System Architecture

A. RF System Architecture

The MMIC used for the multichannel imaging radar is described in [7]. The architecture is optimized for a low PN in a single-channel radar measurement. Therefore, it uses a low-frequency multiplier with factor 4 for the FMCW ramp oscillator (RO) and a low PN LO for the upconversion to the operating frequency at 160 GHz. The fed-in ramp signal from 8-to-12 GHz is multiplied by 4 to 32-to-48 GHz on the MMIC itself (see Fig. 1). The ramp signal from 8-to-12 GHz can be realized with an off-the-shelf fractional-N PLL and an external wideband VCO with a low PN.

The LO signal is generated on each MMIC by an on-chip integer-N PLL, which is used for upconversion of the ramp signal. The reference frequency of the on-chip PLL is a surface-acoustic wave (SAW) oscillator at 916 MHz with a PN of −150 dBc/Hz at 100-kHz offset frequency. This frequency is increased by a factor of 128 resulting in an LO frequency of about 117 GHz. It is already shown in [7] that the PN density of the realized on-chip integer-N PLL is comparable to the swept fractional-N PLL (RO) due to the high-frequency reference and a VCO with a narrow bandwidth. Therefore, the LO only marginally contributes to the overall PN of the TX signal for offset frequencies between 100 kHz and 1 MHz.

The ramp signal from 8-to-12 GHz, multiplied by 4, is upconverted with the fixed-frequency LO to the radio frequency (RF) band from 149-to-165 GHz. The upconverted signal is splitted and fed to the TX and the RX path. Two dielectric resonator antennas (DRAs) are used, which are excited with short-circuited quarter-wavelength patches [7].

The single-channel MMIC is coherently extended to an eight-channel imaging radar system as depicted in Fig. 1. This is realized by distributing the ramp signal and the SAW reference to all eight radar MMICs. The antennas are aligned in a row in the E-plane (xy plane), and a dielectric spherical-convex lens made of Teflon [polytetrafluoroethylene (PTFE)] with ε_r=2.1, a diameter of D_L=38.6 mm, and a focal distance d_f = 2 cm is used to focus the radiation pattern in the H-plane (yz plane). As the antennas are in one row, no gain reduction due to a parallax of an imperfect focusing lens has to be taken into account [17]. The measured radiation pattern of the lens antenna at the center frequency f_c = 154 GHz is shown in Fig. 2. The lens design has a 3-dB-beamwidth of $\varphi_\mathrm{3dB}\approx 5°$ in the H-plane, whereas no focusing is realized in the E-plane.

B. Noise Mechanism in Radar Systems

The noise level in the sampled intermediate frequency (IF) signal limits the achievable signal-to-noise ratio (SNR) and is determined by a superposition of thermal noise, quantization noise, and PN. The different noise sources are briefly discussed in general.

1) Thermal Noise: The thermal noise power density after the receiver is given by

$$w_\mathrm{th,in} = k_\mathrm{B} T_\mathrm{e} G_\mathrm{RX} = k_\mathrm{B}(F-1) T_0 G_\mathrm{RX} \tag{1}$$

with the receiver noise figure F, Boltzmann's constant k_B, the receiver noise temperature T_e, the receiver gain G_RX, and the temperature T_0=290 K [18].

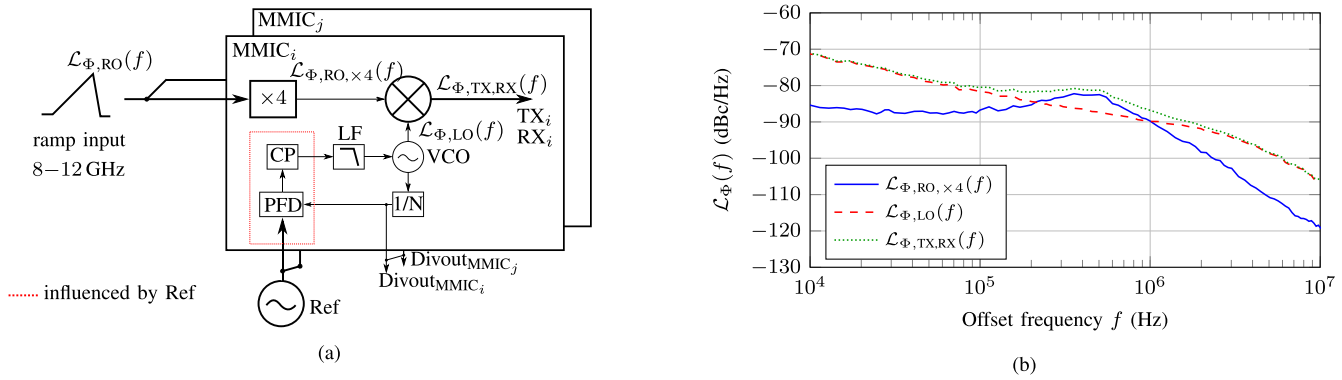

Fig. 3. (a) Block chart of the PLL components affecting the PN of the TX signal. (b) Measured PN densities before and after the upconverting mixer.

2) Quantization Noise: The IF signal is digitized with an analog-to-digital converter (ADC). The maximum achievable SNR due to a quantization is dependent on the number of bits k and is given by $\mathrm{SNR}_{\max} = (6.02 \cdot k + 1.76)$ dB [19].

3) Phase Noise: For most of the PLL components like the loop filter (LF), the VCO, the phase–frequency detector (PFD), as well as the charge pump (CP), the thermal noise and the flicker noise are the main contributions to an emerging PN at the output of the frequency synthesizer [20]. For the following derivation, it is assumed that the PN sources are uncorrelated and can be linearly added up [21]. The PN is determined by

$$\mathcal{L}_{\Phi,\mathrm{PLL}}(f) = \mathcal{L}_{\Phi,\mathrm{Ref}}(f) + \mathcal{L}_{\Phi,\mathrm{LF}} + \mathcal{L}_{\Phi,\mathrm{VCO}}(f) + \mathcal{L}_{\Phi,\mathrm{PFD}}(f) + \mathcal{L}_{\Phi,\mathrm{CP}}(f) \quad (2)$$

with the single sideband PN density $\mathcal{L}(f)$. The subscript Ref refers to the reference oscillator of the PLL. If the same LO is used for the TX and the RX signal path, the range correlation effect occurs [22], dependent on the time delay τ within the radar channel. The residual PN density in the RX output spectrum $\mathcal{L}_{\Delta\Phi}(f)$ can then be calculated by [22]

$$\mathcal{L}_{\Delta\Phi}(f) = 2\mathcal{L}_\Phi(f)(1 - \cos(2\pi f \tau)). \quad (3)$$

In (3), $\mathcal{L}_\Phi$ describes the PN density of the TX signal, and f is the frequency offset from the carrier.

An increase in the noise level due to residual PN occurs locally in the vicinity of a very strong target. This reduces the detection sensitivity of weak targets. For normal radar operation, the leakage signal from the TX to the RX is a strong target, which is on the orders of magnitude larger than the received signal passing through the radar channel to the real target [23]. Typical leakage paths are transmit–receive coupler leakage, antenna reflections, or reflections at a radome or lens.

C. Phase Noise Model of the 160-GHz Radar

The components affecting the PN of the TX signal are shown in Fig. 3(a). At the upconverting mixer, the PN densities of the multiplied ramp signal $\mathcal{L}_{\Phi,\mathrm{RO},\times 4}$ and the LO signal $\mathcal{L}_{\Phi,\mathrm{LO}}$ are linearly superimposed [24]. Fig. 3(b) shows the measured PN densities before ($\mathcal{L}_{\Phi,\mathrm{LO}}$, $\mathcal{L}_{\Phi,\mathrm{RO},\times 4}$) and after ($\mathcal{L}_{\Phi,\mathrm{TX,RX}}$) the upconverting mixer. The PN of the LO is measured after the divider output (Divout) and the PN of the ramp signal before the multiplier input. Afterward, they are deteriorated according to their frequency multipliers of 4 and 128 by 12 and 42 dB, respectively, and added up.

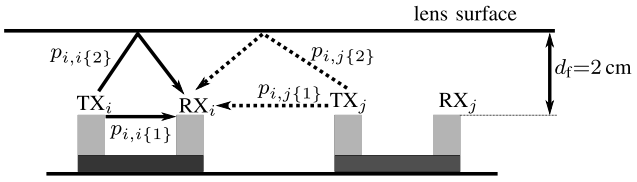

Fig. 4. Possible leakage paths in the multichannel radar.

The decisive leakage paths to be considered for PN are shown in Fig. 4. One is the direct leakage between the two on-chip antennas and the other one is due to the reflection at the lens surface.

In a monostatic radar measurement, i.e., from MMIC$_i$ → MMIC$_i$, with $i \in 1, \ldots, 8$, the same LO is applied for both the transmission and the reception paths. This means that the range correlation effect occurs. The on-chip leakage path has a delay of 33 ps, which results in a PN cancellation factor of 74 dB at 1-MHz offset frequency [25].

For the lens leakage path, an upper bound of the maximum power coupling to the adjacent receive antennas can be approximated by the radar equation for extended targets. In addition, it is assumed that the DRA gain is 6 dBi and that the MMIC output power is P_{out}=−1 dBm. By using Snell's refraction law, the ratio of the reflected wave intensity at the plane dielectric surface can be approximated [26]. For a TEM wave impinging perpendicularly on the air–Teflon interface, about 4%=−14 dB of the power is reflected and couples with a delay of 160 ps and a PN cancellation of 60 dB into the adjacent receivers. A summary of the noise budgets for the monostatic measurements and the system parameters is given in Table II. In addition, it contains the residual PN of both the lens and the DRA leakage for the frequency offset f=1 MHz. They are about 40 dB below the thermal noise power density. Hence, the SNR in the monostatic radar measurement is not degraded due to a residual PN within the leakage signal.

For a bistatic radar measurement from MMIC$_i$→MMIC$_j$, with $i, j \in 1, \ldots, 8, i \neq j$, only the ramp and reference signals are the same for the transmitting and the receiving MMICs.

TABLE II
NOISE BUDGETS FOR THE MONOSTATIC RADAR MEASUREMENT AT 1-MHz OFFSET FREQUENCY

TX power	−1 dBm
DRA gain	6 dBi
RX gain	−2 dB [7]
RX noise figure	25 dB [7]
Thermal noise power density	−151 dBm/Hz
TX signal PN density $\mathcal{L}_{\Phi,\mathrm{TX,RX}}$ (1 MHz)	−87 dBc/Hz
Measured on-chip leakage attenuation $p_{i,i}\{1\}$	29 dB [25]
PN cancellation factor DRA leakage	−74 dB (33 ps) [25]
Residual PN power density DRA leakage	−193 dBm/Hz
Lens leakage attenuation (radar eq. + Snell)	51 dB
PN cancellation factor lens leakage	−60 dB (160 ps)
Residual PN power density lens leakage	−201 dBm/Hz

Thus, the range-correlation effect is only valid for the ramp and the reference signal. It can be assumed that the residual PN density of both the signals is below the thermal noise power density as in the monostatic case.

In comparison with the monostatic case, different PLL components, such as LF, VCO, N-divider, PFD, and CP are involved in the bistatic system operation. Some of the components are affected by the common SAW reference oscillator at 916 MHz. Especially the PFD and the CP pulses are dependent on the common reference frequency. Therefore, there are PLL components with perfect correlation, partial correlation, and with no correlation. The common reference is correlated as it is the same for all on-chip PLLs. The PFD and the CP are partially correlated due to the direct influence of the reference oscillator on the PFD and CP cycle times [see Fig. 3(a)]. Components like the VCO, the LF, and the dividers are fully uncorrelated as there is no relation to the reference oscillator. The PN density at the receiver output spectrum in a measurement from $\mathrm{MMIC}_i \rightarrow \mathrm{MMIC}_j$ can be written as

$$\begin{aligned}\mathcal{L}_{\Delta\Phi_{j,i}}(f) = {} & \mathcal{L}_{\varphi,u_i}(f) + \mathcal{L}_{\varphi,u_j}(f) \\ & + 2(\mathcal{L}_{\varphi,\mathrm{Ref+ramp}}(f) + \mathcal{L}_{\varphi,\mathrm{PLL,corr}}(f)) \\ & \times (1 - \cos(2\pi\,\tau_{j,i}\,f)). \end{aligned} \tag{4}$$

In (4), $\mathcal{L}_{\varphi,u_{i,j}}(f)$ describes the PN density, which results from the uncorrelated PLL components (LF, VCO, and N-divider) and the uncorrelated parts of the PFD and CP in MMIC_i and MMIC_j due to their individual thermal and flicker noise. $\mathcal{L}_{\varphi,\mathrm{Ref+ramp}}(f)$ is the PN density of the reference oscillator and the ramp signal, which is the same for all MMICs and hence correlated, whereas $\mathcal{L}_{\varphi,\mathrm{PLL,corr}}(f)$ is the PN profile resulting from the correlated parts within the PFD and the CP.

To prove the concept of partial correlation in frequency synthesizers using the same reference, the divider outputs of the on-chip frequency synthesizers of two individual MMICs with the same reference are investigated with the measurement setup as given in Fig. 5(a). One of the signals is upconverted using a high-quality oscillator with a superior PN performance $\mathcal{L}_{\Phi,\mathrm{XCO}}$ in comparison with the PN of the divider outputs ($\mathcal{L}_{\Phi,\mathrm{Divout1,2}}$) of the on-chip PLLs. That means that the PN of the divider output is dominating and therefore mainly present after the upconverting mixer. This signal is afterward

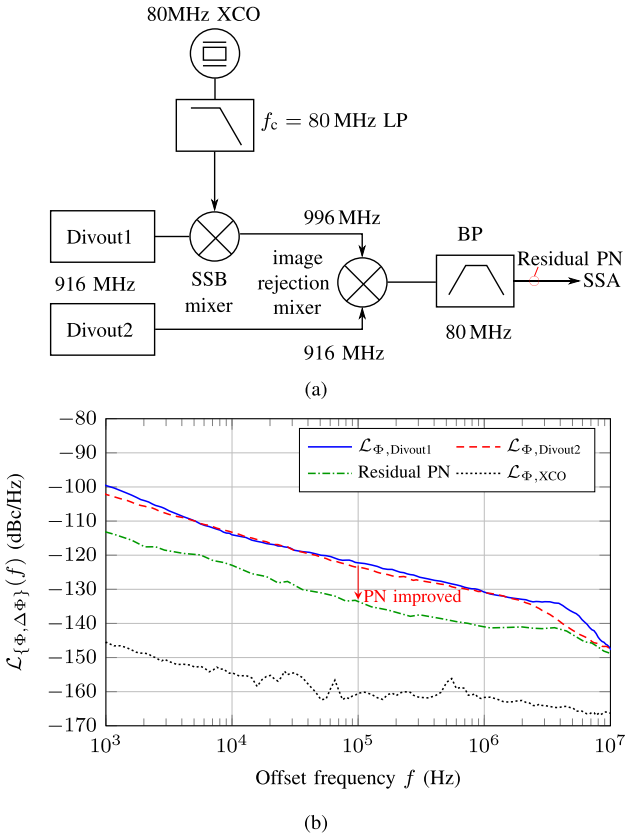

Fig. 5. (a) Block chart of the measurement setup. (b) Measurement results of the residual PN in multiple frequency synthesizers with the same reference.

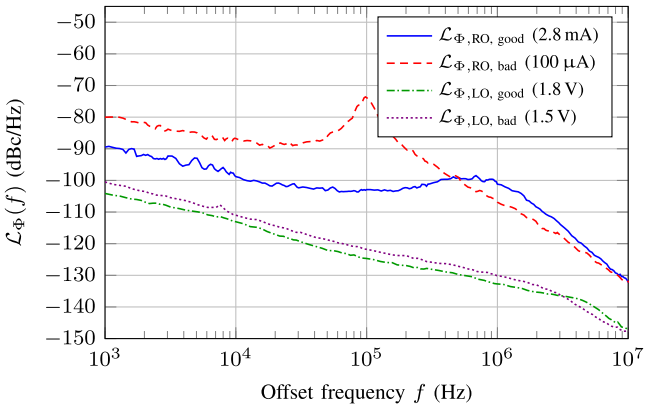

Fig. 6. Measured PN densities for the RO with and without reduced CP current and for the LO with and without reduced power-supply voltage.

downconverted, and the residual PN can be measured by using a signal source analyzer (SSA).

As can be seen in the measurement in Fig. 5(b), the PN is improved, which proves that there are correlated components due to the common reference input. Due to the uncorrelated PLL components in two different MMICs, it might happen that the residual PN density at the receiver output supersedes the thermal noise power density resulting in an increase of the system noise level.

The theory is now proven by radar measurements. Thus, the PN of both the ramp signal and the LO signal is deteriorated as depicted in Fig. 6. For the ramp signal, this is achieved

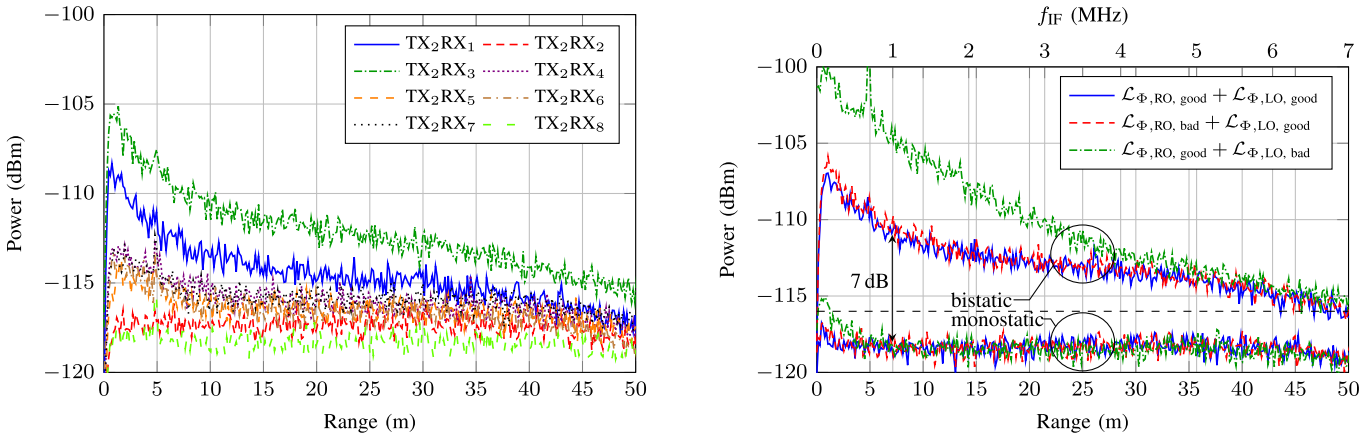

Fig. 7. Noise level for both the monostatic and the bistatic radar cases in comparison. (a) Noise level as a function of the ramp input and LO input PN performance. (b) Noise level dependent on the RX antenna distance. The noise level is dependent on the LO PN performance for the bistatic case. Furthermore, the noise level is mostly increased for the RX antennas spaced next to the active TX antenna as they are affected by the strongest leakage power. Therefore, the SNR for short-range targets is degraded in 56 of 64 virtual channels.

by a reduction in the CP current from 2.8 mA to 100 μA. For the LO, this can be obtained by a reduction in the supply voltage from 1.8 to 1.5 V. Afterward, radar measurements are conducted and statistically evaluated by the standard deviation in the IF signal spectrum over 100 ramps and for each TX channel. The standard deviation is a measure of the noise level within the IF signal.

Fig. 7 shows the noise level—derived from the standard deviation—for both the monostatic and the bistatic radar cases in comparison. For the monostatic case, the noise level is not deteriorated due to a decreased PN performance of both the ramp and the LO signals. In the bistatic radar case in comparison, the noise level is increased by about 7 dB at an IF frequency $f_{\mathrm{IF}} = 1$ MHz as depicted in Fig. 7(a). However, the bistatic radar case is not affected by a deterioration in ramp signal PN of approximately 25 dB [see Figs. 6 and 7(a)]. By deteriorating the PN performance of the LO, the standard deviation and therefore the noise level increase for a low IF in the bistatic case. This can be explained by the uncorrelated PN caused by the different on-chip PLLs.

This effect also holds for the other receive channels and depends on the MMIC distance among each other as can be seen in Fig. 7(b) for all eight virtual channels belonging to TX_2. The larger the RX antenna distance compared with the active TX antenna (see Fig. 8), the less power couples to it. For the largest leakage power, the noise level is increased by approximately 10 dB. Therefore, the increase in noise level is larger for the adjacent MMICs. The measurements show that RX_3, which is next to TX_2, perceives the largest increase in noise level.

III. Antenna Array Optimization

Multiple-input multiple-output (MIMO) radars are typically realized with uniform linear arrays (ULAs) and an interelement spacing of $\lambda/2$. This approach has a maximum sidelobe level (SLL) suppression of -13.3 dB and avoids grating lobes within the angular range $\pm 90°$ [27]. By using fully integrated radar MMICs with AoCs, it is usually not possible to realize an interelement spacing of $\lambda/2$, because PCB and MMIC interconnect constraints have to be fulfilled. In the following section, an optimization criterion, which considers an MMIC spacing of several wavelengths including manufacturing tolerances, is derived.

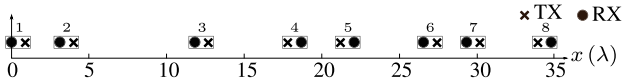

Fig. 8. Realized array geometry. The MMICs are marked by rectangles.

A. Boundary Conditions

The above-mentioned boundary conditions concerning the alignment of the radar MMICs to realize the 8×8 MIMO radar result from the following reasons. The MMICs comprise a TX and an RX antenna with a fixed antenna distance of 0.87 λ on-chip. In addition, the MMIC has different digital interconnects and two RF signals like the 916-MHz SAW reference and the ramp signal, which have to be fed to the MMIC. Due to PCB routing constraints, the MMICs can only be placed with a distance of several wavelengths next to each other. The spacing constraints were experimentally determined and are as follows.

1) *TX* $\longleftrightarrow$ *TX:* 4.1 mm = 2.2 λ.
2) *RX* $\longleftrightarrow$ *RX:* 2.8 mm = 1.5 λ.
3) *TX* $\longleftrightarrow$ *RX:* 3.6 mm = 1.9 λ.

Nevertheless, it is possible to achieve interelement antenna spacings of less than $\lambda/2$ within the virtual array (see Section III-C).

B. Design Criterion and Optimization Algorithm

The array alignment is optimized using a genetic algorithm (GA). The implemented algorithm is adapted from [28] and [29]. The allowed MMIC positions are discretized with a grid of 0.1 λ within the simulation. Within this

grid, the TX antenna position is chosen randomly, and the corresponding RX antenna is placed 0.87 λ with respect to the TX antenna. Afterward, the agreement to the constraints in Section III-A is verified.

In order to rank and compare the resulting array configuration, a maximum allowed array size and a minimum required angular resolution has to be specified. It is defined with the Rayleigh criterion [30]

$$\Delta\varphi = 1.22\frac{\lambda}{d_{\mathrm{V}}} \quad . \tag{5}$$

The angular resolution in radiant is described by $\Delta\varphi$, and d_{V} is the virtual aperture size of the antenna array. For a desired angular resolution of 1°, the necessary virtual aperture size is $d_{\mathrm{V}}{\approx}70\ \lambda$ resulting in a physical aperture size of $d_{\mathrm{A}}{\approx}35\ \lambda$.

The used DRAs provide a measured 6-dB beamwidth of about ±40° [7]. Therefore, the fitness function f_{n} to rank the found arrays is evaluated within this angular range by

$$f_{\mathrm{n}} = \frac{1}{\text{ambiguity-free region}}\mathrm{SLL}_{\max} \quad . \tag{6}$$

The ambiguity-free region is defined as the angular range for which the SLL is below 0.5=−6 dB. The ambuiguity-free region is evaluated by the ambiguity function (AF) [31], [32], which is defined by

$$\mathrm{AF}(\varphi_i, \varphi_j) = \frac{|\mathbf{v}(\varphi_i)^H \mathbf{v}(\varphi_j)|}{\| \mathbf{v}(\varphi_i) \| \| \mathbf{v}(\varphi_j) \|} \quad . \tag{7}$$

In (7), $(\cdot)^H$ denotes the Hermitian operator, $\| \cdot \|$ is the Euclidian norm of a vector, and $\mathbf{v}(\varphi) = \mathbf{a}(\varphi) \otimes \mathbf{b}(\varphi)$ is the virtual steering vector, which is given by the Kronecker product $\otimes$ of the transmitter and receiver steering vectors $\mathbf{a}(\varphi)$ and $\mathbf{b}(\varphi)$ [33].

In comparison with [29], the fitness function f_{n} is extended by a weighting with the maximum $\mathrm{SLL}_{\max}$ of the antenna pattern. Thus, arrays with a lower SLL get a higher rank resulting into more robust arrays.

C. Robustness Analysis

At mm-wave frequencies around 160 GHz, the ratio between positioning tolerances and the wavelength is significant and cannot be neglected anymore. In order to realize a robust antenna design without ambiguities, it is necessary to include these tolerances into the array design process. For each array fulfilling the constraints, a Monte Carlo analysis consisting of 1000 randomly modified antenna arrays is added to the optimization algorithm. The antenna positioning variance is modeled by a random Gaussian process with a standard deviation of 50 μ m. The robustness is defined by the percentage of array realizations with full ambiguity-free region in the angular range ±40°. The final array configuration has a simulated maximum $\mathrm{SLL}_{\max}$=−9 dB. For the found antenna array, all the performed Monte Carlo simulations fulfilled the robustness criterion.

Figs. 8 and 9 show the realized array and the corresponding virtual antenna array. The realized antenna positions are measured using a measurement microscope. The values are summarized in Table III and show that the design specifications are met.

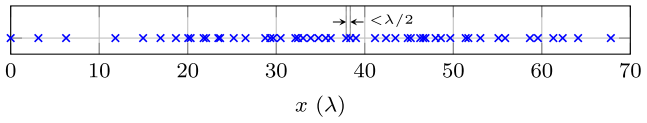

Fig. 9. Simulated virtual array. The virtual RX channels are marked by crosses. Several interelement spacings are lesser than $\lambda/2$.

TABLE III
OVERVIEW OF MEASURED ANTENNA ARRAY

$N_{\{\mathrm{T,R}\}}$ (#)	$x_{\mathrm{R,sim}}$ (mm)	$x_{\mathrm{R,phys}}$ (mm)	Δx_{R} (mm)	$x_{\mathrm{T,sim}}$ (mm)	$x_{\mathrm{T,phys}}$ (mm)	Δx_{T} (mm)
1	0	0	0	1.63	1.68	0.05
2	5.87	5.82	−0.05	7.50	7.50	0
3	22.17	22.15	−0.02	23.80	23.78	−0.02
4	34.98	34.98	0	33.35	33.33	−0.02
5	41.35	41.35	0	39.72	39.72	0
6	49.71	49.71	0	51.34	51.36	0.02
7	54.96	54.95	−0.01	56.59	56.59	0
8	65.16	65.13	−0.02	63.52	63.50	−0.02

D. Array Calibration and Measured Array Performance

Phase and amplitude mismatches between the channels require a calibration. Each virtual channel is formed by a TX_k-RX_l combination. For a single target in the far-field of the antenna array, the phase progression $\Delta\phi_{kl}$ of the (k, l)th virtual antenna element relative to the (1, 1)th virtual antenna element behaves according to

$$\Delta\phi_{kl}(\varphi) = \frac{2\pi}{\lambda}\Delta x_{kl}\sin(\varphi) + \phi_{kl} \tag{8}$$

with the relative virtual antenna distance $\Delta x_{kl}{=}x_{kl}{-}x_{11}$ concerning the virtual receive antenna (1, 1) and the constant phase offset ϕ_{kl}.

Due to manufacturing tolerances, the ideal antenna positions from the simulations slightly differ from the physical realized ones (see Table III).

The array is calibrated in the angular range $-60° \leq \varphi \leq 60°$ with a step size of 0.1°. Fig. 10 shows the measured relative phase progressions and the corresponding target power in dBm as a function of $\sin(\varphi)$.

From the slopes of the curves and by applying (8), the electrical virtual antenna positions coinciding with the electrical antenna behavior are determined. Mutual coupling and other nonidealities shift the physical antenna positions resulting in a larger deviation between ideal and electrical antenna positions (see Fig. 11). From now on, the measured electrical virtual antenna positions are used. For the simulated antenna array, there are 51 unique antenna array positions, whereas for the realized array, 64 virtual antenna elements are obtained due to manufacturing tolerances and coupling effects.

With the measured virtual antenna array steering matrix from Fig. 10(a) and (b), the AF in (7) can be calculated (see Fig. 12). There are no ambiguities within the azimuth angular range of ±60°.

IV. IMAGING PERFORMANCE

A. Measurement System

The radar system is realized in a modular PCB stack, with each functional part on a separate PCB to achieve modularity

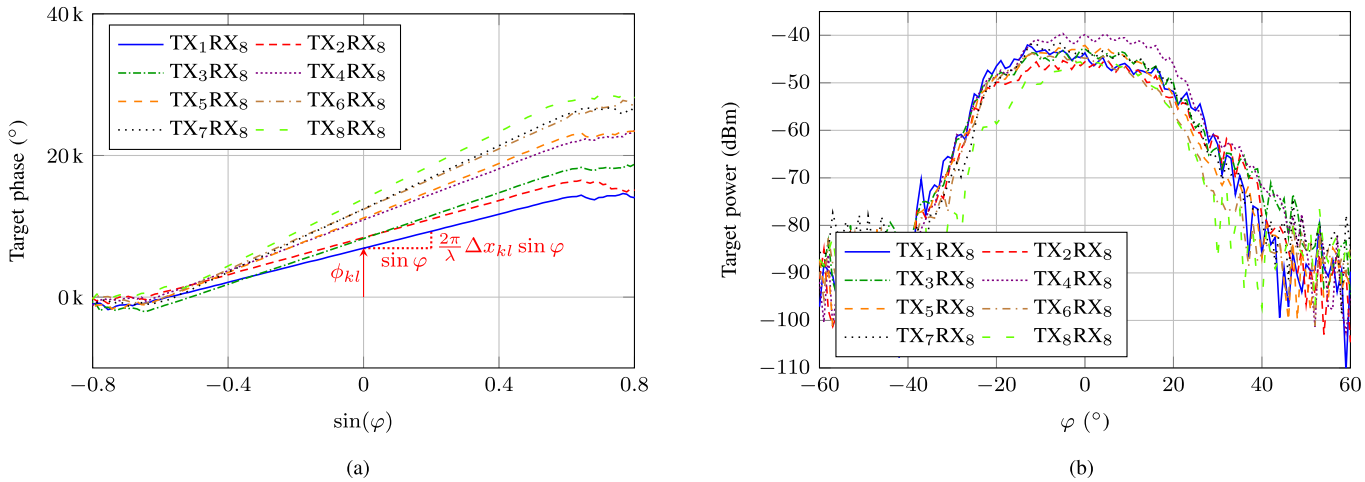

Fig. 10. (a) Measured relative phase progression and (b) amplitude variations for one target placed at a distance of R=5 m exemplarily shown for the virtual channels belonging to RX_8.

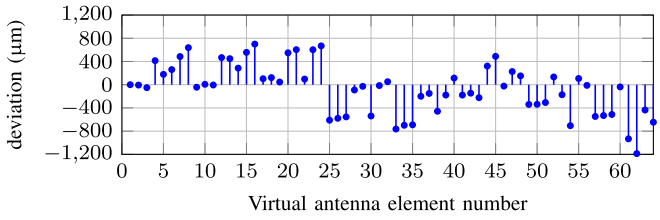

Fig. 11. Deviation of electrical from ideal virtual RX positions.

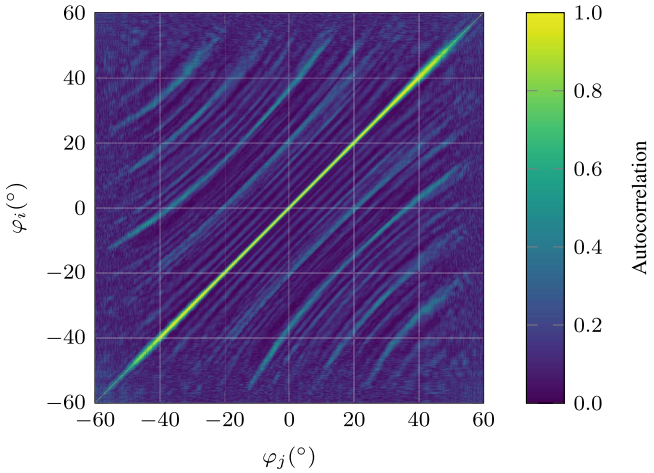

Fig. 12. Measured AF. The array has a full ambiguity-free region (<0.5) within [−60°, 60°].

and to facilitate error diagnostics. The radar stack is subdivided into an RF PCB comprising the MMICs and the RF signal lines below 12 GHz, a PLL PCB for the ramp generation, an IF PCB with a variable amplification from 34 to 52 dB for eight differential channels, and a power supply PCB with a microcontroller (μC) as depicted in Fig. 13.

B. Phase Ambiguities

The used integer-N PLLs ensure that the relative output phases between the different VCOs are deterministic. Consequently, a phase synchronization is avoided and the underlying system architecture is capable of imaging. In comparison, fractional-N PLLs result in phase ambiguities [21].

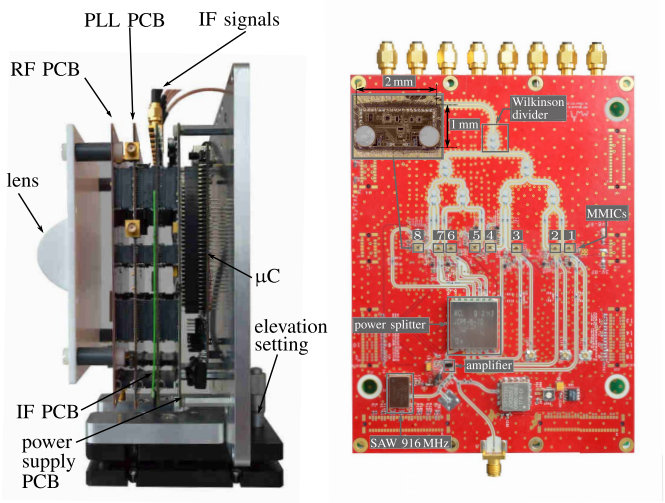

Fig. 13. Photographs of (a) modular radar stack and (b) RF PCB zoomed-in view of an MMIC.

TABLE IV
OVERVIEW OF THE RADAR SETTINGS

Ramp duration T	100 µs
Ramp repetition time T_r	150 µs
Ramp start frequency f_{start}	8 GHz
Ramp stop frequency f_{stop}	10.5 GHz
RF bandwidth B	10 GHz
Center frequency f_c	154 GHz
Number of chirps N_c	512

C. Angular Resolution

In order to demonstrate the imaging capabilities, radar measurements are conducted with the parameters summarized in Table IV. The angular resolution for the case of two targets with the same image intensity can be determined by (5). For the realized array and for the operated center frequency f_c=154 GHz, the calculated angular resolution is 1.06°.

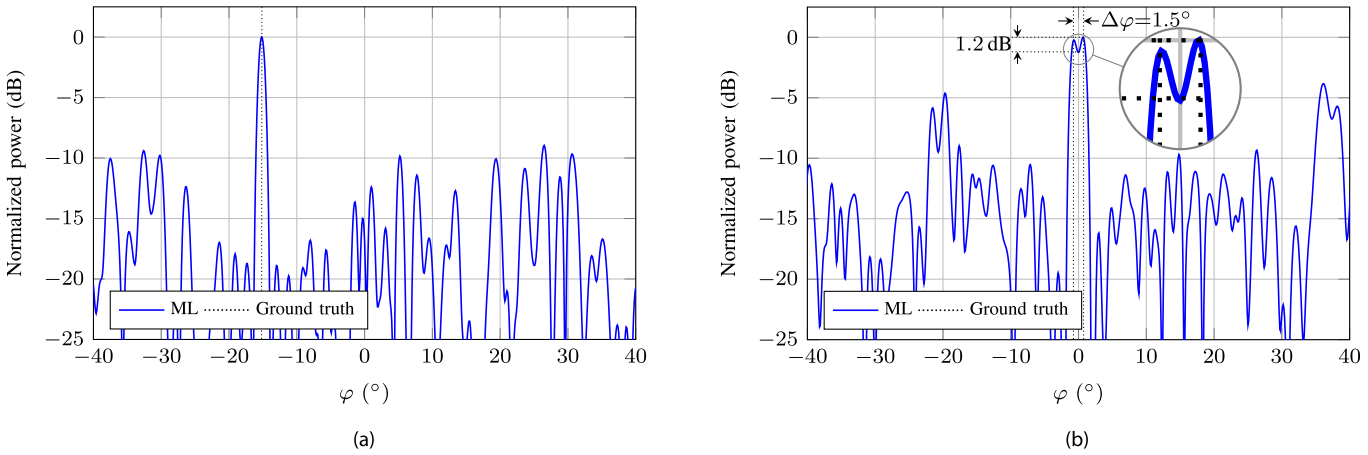

Fig. 14. Measured angular estimation performance of the realized antenna array for (a) one target at φ=−15° and (b) two targets with an angular separation of $\Delta\varphi$=1.5°.

The measurements are evaluated using the maximum likelihood (ML) method, which correlates the measurement vector with the interpolated calibration vectors. Fig. 14(a) shows one single target at the angle φ=−15°, whereas Fig. 14(b) shows the separability performance of two targets of the same image intensity and with an angular separation of 1.5°. Both the targets can be separated with a notch of 1.2 dB. The angular resolution of 1.5° is close to the theoretical limit of 1.06°.

D. Time-Division Multiplexing

The radar system uses time-division multiplexing (TDM) to transmit orthogonal waveforms for MIMO. This reduces the maximum detectable Doppler frequency $f_{\mathrm{D,max}}$ by the number of transmit antennas, because the Doppler frequency f_{D} is only sampled by every eighth transmitted ramp [27]. Furthermore, an additional phase difference of $\Delta\phi_{\mathrm{TDM}}=2\pi f_{\mathrm{D}} T_r$ due to the switching time occurs, which is corrected by an adapted discrete Fourier transform as in [34]. The time T_r denotes the ramp repetition time between two consecutive ramp segments.

V. Radar Measurements of Extended Targets

To evaluate the radar performance in realistic scenarios, two well-defined nonstationary scenarios are investigated. The first scenario consists of four metallic cylinders with diameter 1.6 cm mounted on a wooden plate with the dimensions 25 cm ×19 cm ($l\times w$), whereas the second scenario is a metallic cuboid with the dimensions 45 cm×30 cm×30 cm ($l\times w\times h$). Both the targets are rotating with a radial velocity v_{r}=50°/s around their vertical axis. The measurement scenarios are depicted in Fig. 15. The virtual channels are noncoherently integrated. After separating the targets in the range–velocity domain (R-v-domain), an ML angle estimation is performed and the maximum value within the angular spectrum is determined and marked in an x–y diagram.

A. Scenario 1: Metallic Cylinders

The power range profile of the measured cylinders is depicted in Fig. 16. The results of the measurements are shown in Fig. 17. The orientation of the four cylinders and the

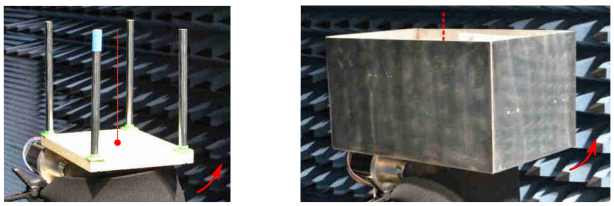

Fig. 15. Photographs of the measured scenarios. (a) First scenario: four metallic cylinders are mounted on a wooden plate and rotated around its vertical axis. (b) Second scenario: cylinders are replaced by a metallic cuboid. The rotation axis and the direction are indicated with red.

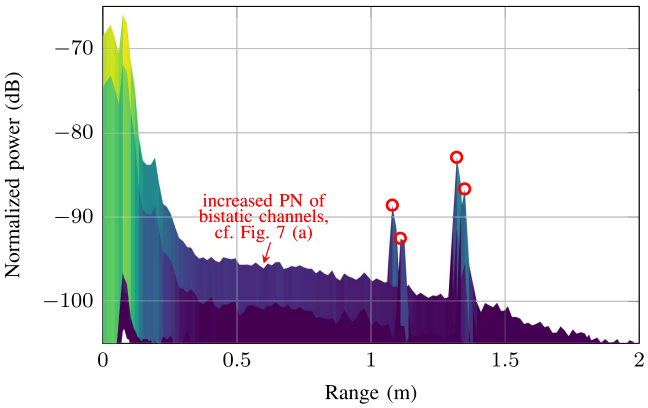

Fig. 16. Power range profile of scenario 1. The large absolute bandwidth enables to separate the cylinders in range.

distance to each other can be estimated with high accuracy. It is possible to separate the four targets independently both in range and velocity [see Figs. 16 and 17(a)]. The noise level is increased at v=0 m/s due to the decreased PN performance within the bistatic channels [see also Fig. 7(a)].

B. Scenario 2: Metallic Cuboid

The measurements in Fig. 18 show that the dynamic range of the radar enables to detect diffracting sharp edges. The x–y diagram in Fig. 18(b) shows that it is even possible to determine the orientation of the cuboid assuming a prior knowledge about both side lengths.

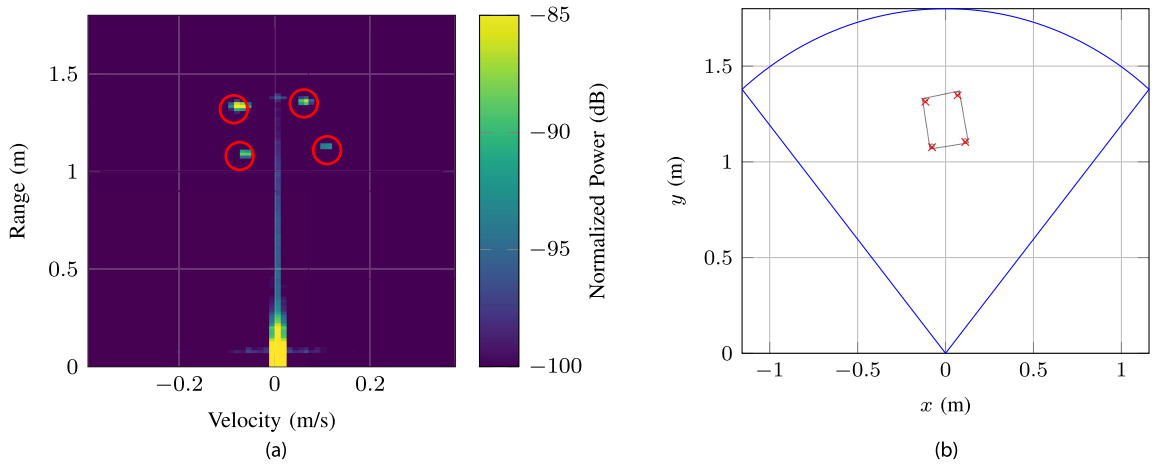

Fig. 17. Imaging results consisting of (a) R–v diagram and (b) x–y diagram for the four rotating metallic cylinders around its axis. The orientation of the four cylinders can be determined.

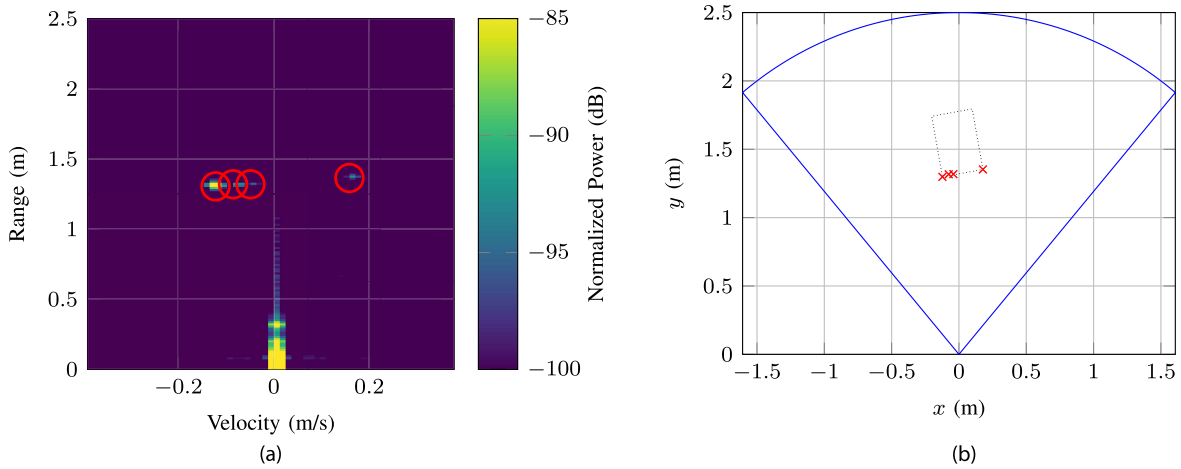

Fig. 18. Imaging results consisting of (a) R–v diagram and (b) x–y diagram for a rotating metallic cuboid. Both edges and two direct reflections at the surface are measured and can be independently separated in range and velocity.

The measurement results in Figs. 17 and 18 verify the good imaging capability of the realized radar system.

VI. Conclusion

In this paper, a 160-GHz high-resolution imaging radar system with simple single-channel radar MMICs at 160 GHz is shown. The MMICs use an on-chip PLL for frequency synthesis. A corresponding PN analysis is presented and proven by radar measurements. A monostatic radar measurement is limited by thermal noise, and the bistatic radar measurements are affected by the PN occurring due to the lens leakage, which increases the system noise level. This effect is dependent on the power coupling to the receivers and is more distinct for the adjacent receive antennas. In addition, a very robust array design including manufacturing tolerances is proposed resulting in a highly sparse antenna array with sidelobes below -9 dB, an ambiguity-free region of $\pm 60°$, and a high angular resolution of 1.5°. The high-resolution imaging capabilities of the realized radar system are demonstrated using two exemplary nonstationary scenarios with the possibility to separate the targets independently in range and velocity.

References

[1] R. Lachner, "Industrialization of mmWave SiGe technologies: Status, future requirements and challenges," in *Proc. 13th Top. Meeting Silicon Monolithic Integr. Circuits RF Syst.*, Jan. 2013, pp. 105–107.

[2] I. Sarkas, J. Hasch, A. Balteanu, and S. P. Voinigescu, "A fundamental frequency 120-GHz SiGe BiCMOS distance sensor with integrated antenna," *IEEE Trans. Microw. Theory Techn.*, vol. 60, no. 3, pp. 795–812, Mar. 2012.

[3] M. G. Girma, J. Hasch, M. Gonser, Y. Sun, and T. Zwick, "122 GHz single-chip dual-channel SMD radar sensor with integrated antennas for distance and angle measurements," in *Proc. 11th Eur. Radar Conf.*, Oct. 2014, pp. 1754–1757.

[4] T. Jaeschke, C. Bredendiek, and N. Pohl, "A 240 GHz ultra-wideband FMCW radar system with on-chip antennas for high resolution radar imaging," in *IEEE MTT-S Int. Microw. Symp. Dig.*, Jun. 2013, pp. 1–4.

[5] S. Yuan, A. Strodl, V. Valenta, A. Trasser, and H. Schumacher, "Compact 120-140 GHz radar Tx/Rx sensors with on-chip antenna," in *Proc. IEEE Radio Wireless Symp. (RWS)*, Jan. 2014, pp. 79–81.

[6] J. Grzyb, K. Statnikov, N. Sarmah, B. Heinemann, and U. R. Pfeiffer, "A 210–270-GHz circularly polarized FMCW radar with a single-lens-coupled SiGe HBT chip," *IEEE Trans. THz Sci. Technol.*, vol. 6, no. 6, pp. 771–783, Nov. 2016.

[7] M. Hitzler *et al.*, "Ultracompact 160-GHz FMCW radar MMIC with fully integrated offset synthesizer," *IEEE Trans. Microw. Theory Techn.*, vol. 65, no. 5, pp. 1682–1691, May 2017.

[8] W. Mayer, A. Gronau, W. Menzel, and H. Leier, "A compact 24 GHz sensor for beam-forming and imaging," in *Proc. 9th Int. Conf. Control, Automat., Robot. Vis.*, Dec. 2006, pp. 1–6.

[9] H. J. Ng, W. Ahmad, and D. Kissinger, "Scalable MIMO radar utilizing delta-sigma modulation-based frequency-division multiplexing technique," in *Proc. Eur. Radar Conf. (EURAD)*, Oct. 2017, pp. 118–121.

[10] Z. Peng and C. Li, "A portable K-band 3-D MIMO radar with nonuniformly spaced array for short-range localization," *IEEE Trans. Microw. Theory Techn.*, vol. 66, no. 11, pp. 5075–5086, Nov. 2018.

[11] R. Feger, C. Wagner, S. Schuster, S. Scheiblhofer, H. Jager, and A. Stelzer, "A 77-GHz FMCW MIMO radar based on an SiGe single-chip transceiver," *IEEE Trans. Microw. Theory Techn.*, vol. 57, no. 5, pp. 1020–1035, May 2009.

[12] D. Zankl *et al.*, "BLASTDAR—A large radar sensor array system for blast furnace burden surface imaging," *IEEE Sensors J.*, vol. 15, no. 10, pp. 5893–5909, Oct. 2015.

[13] A. J. Kirschner, J. Guetlein, S. Bertl, and J. Detlefsen, "A millimetre-wave MIMO radar system for threat detection in patrol or checkpoint scenarios," in *Proc. IET Int. Conf. Radar Syst.*, Oct. 2012, pp. 1–6.

[14] D. Bleh *et al.*, "W-Band time-domain multiplexing FMCW MIMO radar for far-field 3-D imaging," *IEEE Trans. Microw. Theory Techn.*, vol. 65, no. 9, pp. 3474–3484, Sep. 2017.

[15] S. Kueppers, H. Cetinkaya, and N. Pohl, "A compact 120 GHz SiGe:C based 2×8 FMCW MIMO radar sensor for robot navigation in low visibility environments," in *Proc. Eur. Radar Conf. (EURAD)*, Oct. 2017, pp. 122–125.

[16] T. Spreng, S. Yuan, V. Valenta, H. Schumacher, U. Siart, and V. Ziegler, "Wideband 120 GHz to 140 GHz MIMO radar: System design and imaging results," in *Proc. Eur. Microw. Conf. (EuMC)*, Sep. 2015, pp. 430–433.

[17] J. L. Volakis, *Antenna Engineering Handbook*. New York, NY, USA: McGraw-Hill, 2007.

[18] D. Pozar, *Microwave Engineering*, 4th ed. Hoboken, NJ, USA: Wiley 2012.

[19] M. J. Pelgrom, *Analog-to-Digital Conversion*, 2nd ed. New York, NY, USA: Springer, 2012.

[20] H. Arora, N. Klemmer, J. C. Morizio, and P. D. Wolf, "Enhanced phase noise modeling of fractional-N frequency synthesizers," *IEEE Trans. Circuits Syst. I, Reg. Papers*, vol. 52, no. 2, pp. 379–395, Feb. 2005.

[21] D. Banerjee, *PLL Performance, Simulation, and Design*, 4th ed. Indianapolis, IN, USA: Dog Ear Publishing, 2006.

[22] M. C. Budge and M. P. Burt, "Range correlation effects in radars," in *Proc. IEEE Nat. Radar Conf.*, Apr. 1993, pp. 212–216.

[23] G. M. Brooker, "Understanding millimetre wave FMCW radars," in *Proc. 1st Int. Conf. Sens. Technol.*, Nov. 2005, pp. 152–157.

[24] K. V. Puglia, "Phase noise analysis of component cascades," *IEEE Microw. Mag.*, vol. 3, no. 4, pp. 71–75, Dec. 2002.

[25] M. Hitzler, P. Grüner, L. Boehm, W. Mayer, and C. Waldschmidt, "On monostatic and bistatic system concepts for mm-wave radar MMICs," *IEEE Trans. Microw. Theory Techn.*, vol. 66, no. 9, pp. 4204–4215, Sep. 2018.

[26] M. Bass, *Handbook of Optics–Geometrical and Physical Optics, Polarized Light, Components and Instruments*. New York, NY, USA: McGraw-Hill, 2009.

[27] J. Li and P. Stoica, "MIMO radar with colocated antennas," *IEEE Signal Process. Mag.*, vol. 24, no. 5, pp. 106–114, Sep. 2007.

[28] R. L. Haupt, "An introduction to genetic algorithms for electromagnetics," *IEEE Antennas Propag. Mag.*, vol. 37, no. 2, pp. 7–15, Apr. 1995.

[29] C. Vasanelli, R. Batra, and C. Waldschmidt, "Optimization of a MIMO radar antenna system for automotive applications," in *Proc. 11th Eur. Conf. Antennas Propag. (EUCAP)*, Mar. 2017, pp. 1113–1117.

[30] E. Hecht, *Optics*, 5th ed. Harlow, U.K.: Pearson, 2017.

[31] C. M. Schmid, R. Feger, C. Pfeffer, and A. Stelzer, "Motion compensation and efficient array design for TDMA FMCW MIMO radar systems," in *Proc. 6th Eur. Conf. Antennas Propag. (EUCAP)*, Mar. 2012, pp. 1746–1750.

[32] C. M. Schmid, C. Pfeffer, R. Feger, and A. Stelzer, "An FMCW MIMO radar calibration and mutual coupling compensation approach," in *Proc. Eur. Radar Conf.*, Oct. 2013, pp. 13–16.

[33] I. Bekkerman and J. Tabrikian, "Target detection and localization using MIMO radars and Sonars," *IEEE Trans Signal Process.*, vol. 54, no. 10, pp. 3873–3883, Oct. 2006.

[34] J. Bechter, F. Roos, and C. Waldschmidt, "Compensation of motion-induced phase errors in TDM MIMO radars," *IEEE Microw. Wireless Compon. Lett.*, vol. 27, no. 12, pp. 1164–1166, Dec. 2017.

André Dürr (S'18) received the M.Sc. degree from Ulm University, Ulm, Germany, in 2017, where he is currently pursuing the Ph.D. degree.

From 2015 to 2016, he was an Intern with the Bosch Research and Technology Center, Palo Alto, CA, USA. In 2017, he joined the Institute of Microwave Engineering, Ulm University. His current research interests include novel imaging radar sensor concepts, phase noise mitigation, and performance degradation of noncoherent multichannel radar systems and their synchronization, all at millimeter-wave frequencies.

Mr. Dürr was a recipient of the Argus Science Award in 2015, the VDE Award in 2015, and the VDI Award in 2017.

Dominik Schwarz received the M.Sc. degree from Ulm University, Ulm, Germany, in 2018, where he is currently pursuing the Ph.D. degree.

From 2011 to 2018, he was an Intern with Hensoldt Sensors, Ulm. In 2018, he joined the Institute of Microwave Engineering, Ulm University. His current research interests include automotive multiple-input multiple-output radars with a focus on high bandwidths, high channel counts, and novel multilayer PCB structures.

Mr. Schwarz was a recipient of the IfKom Award in 2016.

Stephan Häfner received the M.Sc. degree in computer engineering from Technische Universität Ilmenau, Ilmenau, Germany, in 2012, where he is currently pursuing the Ph.D. degree.

Since 2012, he has been with the Electronic Measurement Research Laboratory, Technische Universität Ilmenau. His current research interests include array signal processing and high-resolution parameter estimation for channel sounding and radar applications.

Martin Geiger (GS'16) received the M.Sc. degree from Ulm University, Ulm, Germany, in 2015, where he is currently pursuing the Ph.D. degree.

In 2016, he joined the Institute of Microwave Engineering, Ulm University. His current research interests include novel radar sensor concepts with flexible antennas, dielectric waveguides, and monolithic microwave integrated circuit interconnects, all at millimeter-wave frequencies.

Mr. Geiger was a recipient of the Best Student Paper Award of the 2018 International Microwave Symposium.

Fabian Roos (S'15) received the M.Sc. degree from the Karlsruhe Institute of Technology, Karlsruhe, Germany, in 2014. He is currently pursuing the Ph.D. degree at the Institute of Microwave Engineering, Ulm University, Ulm, Germany.

His current research interests include adaptivity and automotive radar signal processing for chirp-sequence radar.

Martin Hitzler (S'13–M'19) received the Dipl.Ing. degree in electrical engineering from Ulm University, Ulm, Germany, in 2012, where he is currently pursuing the Ph.D. degree at the Institute of Microwave Engineering.

In 2019, he joined MBDA Deutschland GmbH, Schrobenhausen, Germany, where he is responsible for current and future radar systems. He has design and system experience in the fields of millimeter-wave modules, front ends, and antennas for sensor applications. He is experienced in the evaluation of complex components, subsystems, and systems. His current research interests include pulse and FMCW radar sensors, integrated antennas, and monolithic microwave integrated circuit packaging and interconnects.

Dr. Hitzler was a recipient of the Advanced Research Group Uniting Super-Humans Science Award in 2013. He serves as a Reviewer for several IEEE TRANSACTIONS and LETTERS.

Philipp Hügler (S'15) received the M.Sc. degree in electrical engineering from Ulm University, Ulm, Germany, in 2014, where he is currently pursuing the Ph.D. degree at the Institute of Microwave Engineering (MWT).

His current research interests include closed-up range frequency-modulated continuous wave radar sensors and imaging radar front ends at millimeter-wave frequencies for unmanned aerial vehicle applications.

Reiner Thomä (M'92–SM'99–F'07) received the Dipl.Ing. (M.S.E.E.), Dr. Ing. (Ph.D.E.E.), and Dr. Ing. Habil. degrees in electrical engineering and information technology from the Technische Hochschule Ilmenau, Ilmenau, Germany, in 1975, 1983, and 1989, respectively.

From 1975 to 1988, he was a Research Associate in electronic circuits, measurement engineering, and digital signal processing with Technische Hochschule Ilmenau. From 1988 to 1990, he was a Research Engineer with the Zentrum für Wissenschaftlichen Gerätebau, Akademie der Wissenschaften der DDR, where he was involved in radio surveillance. In 1991, he spent a sabbatical leave with the Lehrstuhl für Nachrichtentechnik, University of Erlangen–Nürnberg, Erlangen, Germany. Since 1992, he has been a Professor of electrical engineering (electronic measurement) with the Technische Universität Ilmenau, where he was the Director of the Institute of Communications and Measurement Engineering from 1999 to 2005. With his group, he has contributed to several European and German research projects and clusters, such as RESCUE, WINNER, PULSERS, EUWB, NEWCOM, COST 273, COST 2100, IC 1004, IRACON, EASY-A, and EASY-C. His current research interests include measurement and digital signal processing methods, such as correlation and spectral analysis, system identification, sensor arrays, compressive sensing, time–frequency analysis, and cyclostationary signal analysis; their application in mobile radio and radar systems, such as multidimensional channel sounding, propagation measurement and parameter estimation, and multiple-input multiple-output (MIMO), mm-wave, and ultra-wideband (UWB) radar; and measurement-based performance evaluation of MIMO transmission systems, including over-the-air testing in virtual electromagnetic environments, passive coherent location, and UWB radar sensor systems for object detection, tracking, and imaging.

Dr. Thomä is a member of the International Union of Radio Science (Commissions A) and VDE/ITG. He became an Advisory Board member of the EU Project mmMAGIC. He was the recipient of the Thuringian State Research Award both for applied research and for contributions to high-resolution multidimensional channel sounding. In 2014, he was the recipient of the Vodafone Innovation Award. Since 1999, he has been serving as the Chair for the IEEE-IM TC-13 on Measurement in Wireless and Telecommunications. He was the Speaker of the German nation-wide Deutsche Forschungsgemeinschaft-focus project Ultra-Wideband Radio Technologies for Communications, Localization and Sensor Applications (UKoLOS) (SPP 1202).

Christian Waldschmidt (S'01–M'05–SM'13) received the Dipl.Ing.(M.S.E.E.) and Dr. Ing. (Ph.D.E.E.) degrees from the Universität Karlsruhe (TH), Karlsruhe, Germany, in 2001 and 2004, respectively.

From 2001 to 2004, he was a Research Assistant with the Institut für Höchstfrequenztechnik and Elektronik (IHE), Universität Karlsruhe (TH). Since 2004, he has been with Robert Bosch GmbH, Gerlingen, Germany, in the Business Unit's Corporate Research and Chassis Systems. He was heading different research and development teams in microwave engineering, RF-sensing, and automotive radar. In 2013, he returned to academia. He was appointed as the Director of the Institute of Microwave Engineering, Ulm University, Ulm, Germany, as a Full Professor. He has authored or co-authored over 150 scientific publications and holds more than 20 patents. His current research interests include radar and RF-sensing, mm-wave and submillimeter-wave engineering, antennas and antenna arrays, and RF and array signal processing.

Dr. Waldschmidt is an Executive Committee Board member of the German MTT/AP Joint Chapter and a member of the ITG Committee Microwave Engineering (VDE). He served as the TPC Chair in 2015 and 2017 and as the Chair of the IEEE MTT-S International Conference on Microwaves for Intelligent Mobility in 2018. He is the Chair of the IEEE MTT-27 Technical Committee for the field wireless-enabled automotive and vehicular applications. Since 2018, he has been serving as an Associate Editor for IEEE MTT MICROWAVE WIRELESS COMPONENTS LETTERS. He is a Reviewer for multiple IEEE TRANSACTIONS and several conferences, such as the IEEE MTT-S IMS and EUMW.